Effect of surface-plasmon polaritons on spontaneous emission and intermolecular energy-transfer rates in multilayered geometries

C. A. Marocico and J. Knoester*

Zernike Institute for Advanced Materials, University of Groningen, Nijenborgh 4, NL-9747 AG Groningen, The Netherlands

(Received 19 August 2011; published 14 November 2011)

We use a Green's tensor method to investigate the spontaneous emission rate of a molecule and the energy-transfer rate between molecules placed in two types of layered geometries: a slab geometry and a planar waveguide. We focus especially on the role played by surface-plasmon polaritons in modifying the spontaneous emission and energy-transfer rates as compared to free space. In the presence of more than one interface, the surface-plasmon polariton modes split into several branches, and each branch can contribute significantly to modifying the electromagnetic properties of atoms and molecules. Enhancements of several orders of magnitude both in the spontaneous emission rate of a molecule and the energy-transfer rate between molecules are obtained and, by tuning the parameters of the geometry, one has the ability to control the range and magnitude of these enhancements. For the energy-transfer rate interference effects between contributions of different plasmon-polariton branches are observed as oscillations in the distance dependence of this rate.

DOI: 10.1103/PhysRevA.84.053824 PACS number(s): 33.80.−b, 42.50.−p, 73.20.Mf

I. INTRODUCTION

The control of electromagnetic properties of molecules, such as their spontaneous emission constant and frequency, and their intermolecular resonance interactions, is a topic of considerable interest, both for fundamental reasons and for applications in (electro)optical devices. One way to control these properties is by chemical modification of the molecule, leading to a change of its electronic level structure. However, the electromagnetic properties may also be influenced without chemical changes, namely by modifying the dielectric and (or) metallic environment of the molecule. The Purcell effect [1] (i.e., the modification of the spontaneous emission rate by the environment) has been known for 75 years by now. Yet, in particular during the past decade, this effect has proven a flourishing area of research, owing to the growing possibilities to control the structure of the environment at the nanometer scale and the increasing precision with which molecules can be positioned within this environment and their properties can be detected. In addition, the desire to control optical signal processing at the nanometer scale (nanophotonics) has boosted activity in this area. A wide variety of geometries has been studied in conjunction with the modification of the spontaneous emission rate: planar metallic and dielectric interfaces [2–5], microcavities [6–10] and multilayered geometries [11], nanorods [12–15], nanospheres [16–19], gratings [20], and photonic crystals [21–27].

Being directly proportional to the local density of electromagnetic states of the environment, the spontaneous emission rate is the most obvious electromagnetic property of atoms and molecules that may be changed by the environment. However, the electromagnetic interactions between molecules, such as the resonance excitation transfer interactions mediated by molecular transition dipoles may also be influenced. This interaction drives the resonant transfer of electronic energy between two molecules and is the main mechanism by which an excited molecule transfers its excitation to a neighboring one. It plays an essential role in a variety of fields, such as microscopy, nanophotonics (LEDs and micro- and nanolasers), and biophysics (photosynthesis) [28]. Within the incoherent limit, the rate of excitation energy transfer is proportional to the square of the dipole-dipole interaction, which in a homogeneous host gives rise to two distance-dependence limits. The first one is the short-range or radiationless regime pioneered by Förster [29], valid when the intermolecular distance R is much smaller than the wavelength associated with the transition of the donor molecule, λ ($R \ll \lambda$). In this limit the transfer-rate scales according to R^{-6} (i.e., the square of the instantaneous Coulomb coupling between two dipoles). The other limit is the long-range or radiative regime [30], valid when $R \gg \lambda$, and having a R^{-2} distance dependence. There also exists an intermediate regime, valid when $R \approx \lambda$, and with a R^{-4} distance dependence.

The transfer of the excitation can always be regarded as proceeding through the exchange of photons. In the Förster regime, these photons are virtual (i.e., appearing only in intermediate states) and are not required to conserve energy, that is, they do not necessarily have the same energy as the molecular transition they facilitate. They have to, however, obey Heisenberg's uncertainty relations for energy and time; therefore, the longer-lived photons (corresponding to molecules further apart) have the smaller permissible spread in energy. When the molecules are a few wavelengths apart, energy conservation is obeyed and the energy-transfer process can be regarded as the emission and absorption of a real photon.

Given the numerous applications of the resonance energy transfer, particularly in the Förster regime, controlled modification of the transfer rate is highly desirable. One way to achieve modifications of the transfer rate is by using inhomogeneous (nanostructured) geometries. Theoretical and experimental work has been carried out in order to study the modifications of the energy-transfer rate in different geometries: planar dielectric interfaces [31,32], microcavities [33–38], dielectric spheres [39–41], nanofibers [42], and the current authors' own contribution on dielectric cylinders [43]. In all cases, both enhancement and inhibition of the transfer rate have been observed and calculated.

*J.Knoester@rug.nl

In Ref. [43] we have shown that surface-plasmon polaritons (SPPs) living at the interface between a dielectric cylinder and its host may have a strong effect on the excitation transfer interactions between molecules placed close to this cylinder. The SPPs may act as intermediate to carry the excitation from one molecule to the other in an efficient way. In this paper we investigate the role that SPPs play in modifying the decay rate of a molecule as well as the energy-transfer rate between two molecules placed inside two types of multilayered structures: a metal slab in a dielectric host and a planar waveguide. The planar waveguide geometry has been considered before [37,38] in a more general case, but without focusing on the role that SPPs might play in modifying the electromagnetic properties of the molecules. One of the interesting differences with the dielectric cylinders in Ref. [43] is that the geometries studied here have more than one interface, each of which may carry SPPs, which in turn may mix if the interfaces are close enough to each other. This yields a variety of SPP branches, each with its own dispersion relation. Depending on distances between the molecules considered and between the molecules and the interfaces, one branch may dominate the effect on the molecules' electromagnetic properties or (in the case of excitation transfer) interference effects between different branches may show up in an oscillatory distance dependence of the rate.

The paper is organized as follows: In Sec. II we give the general formalism for calculating the spontaneous emission and the energy-transfer rates in an inhomogeneous geometry. In order to keep this paper reasonably self-contained, we also briefly introduce SPPs and, for reference, consider the relevant features of these collective excitations for the case of a single planar interface between a semi-infinite metal and a semi-infinite dielectric. In Sec. III the case of a metal (Ag) slab in a dielectric (SiO_2) host is investigated by calculating the spontaneous emission and energy-transfer rates and the SPP contribution to these rates. In Sec. IV a planar waveguide geometry constructed by sandwiching a SiO_2 layer between two Ag plates is considered on the same lines of inquiry. Finally, Sec. V is reserved for conclusions.

II. THEORETICAL FRAMEWORK

A. Electromagnetic interactions, the Green's tensor, and numerical implementation

The *spontaneous emission* (SE) rate of a molecule and the *energy-transfer* (ET) rate between two molecules in any geometry can be calculated using the Green's tensor of the electromagnetic field for that geometry through the following expressions [43–45]:

$$\gamma(\mathbf{r},\omega) = 2\omega^2 d_i\, d_j \mathrm{Im}[\mathcal{G}_{ij}(\mathbf{r},\mathbf{r},\omega)], \tag{1a}$$

for the decay rate of a molecule with electronic transition dipole moment $\mathbf{d}$, transition frequency ω and located at position $\mathbf{r}$ and

$$\Gamma(\mathbf{r}_B,\mathbf{r}_A,\omega) = 2\pi\omega^4 \left| d_B^i \mathcal{G}_{ij}(\mathbf{r}_B,\mathbf{r}_A,\omega) d_A^j \right|^2, \tag{1b}$$

for the energy-transfer rate between two molecules A and B with electronic transition dipole moments $\mathbf{d}_A$ and $\mathbf{d}_B$, transition frequency ω, and located at $\mathbf{r}_A$ and $\mathbf{r}_B$, respectively [46]. The Green's tensor, denoted in the above equations by $\mathcal{G}(\mathbf{r}_A,\mathbf{r}_B,\omega)$, is a solution of the differential equation,

$$\boldsymbol{\nabla}_{\mathbf{r}} \times \boldsymbol{\nabla}_{\mathbf{r}} \times \mathcal{G}(\mathbf{r},\mathbf{s},\omega) - \omega^2 \varepsilon(\mathbf{r},\omega)\mathcal{G}(\mathbf{r},\mathbf{s},\omega) = \mathcal{I}\delta(\mathbf{r}-\mathbf{s}), \tag{2}$$

where $\varepsilon(\mathbf{r},\omega)$ is the position-dependent dielectric permittivity of the geometry at hand and $\mathcal{I}$ is the 3×3 unit tensor. Throughout this paper we have chosen to work in natural units (i.e., $c = \hbar = 1$).

It is useful to consider two other quantities as well, namely the *normalized* spontaneous emission and energy-transfer rates, which are these rates in a specific geometry normalized to their values in free space. By definition, we have

$$\tilde{\gamma}(\mathbf{r},\omega) \equiv \frac{\gamma(\mathbf{r},\omega)}{\gamma_0(\mathbf{r},\omega)} = \frac{\hat{d}_i \hat{d}_j \mathrm{Im}[\mathcal{G}_{ij}(\mathbf{r},\mathbf{r},\omega)]}{\hat{d}_i \hat{d}_j \mathrm{Im}[\mathcal{G}^0_{ij}(\mathbf{r},\mathbf{r},\omega)]}, \tag{3a}$$

$$\tilde{\Gamma}(\mathbf{r}_B,\mathbf{r}_A,\omega) \equiv \frac{\Gamma(\mathbf{r}_B,\mathbf{r}_A,\omega)}{\Gamma_0(\mathbf{r}_B,\mathbf{r}_A,\omega)} = \frac{|\hat{d}_B^i\, \mathcal{G}_{ij}(\mathbf{r}_B,\mathbf{r}_A,\omega)\, \hat{d}_A^j|^2}{|\hat{d}_B^i\, \mathcal{G}^0_{ij}(\mathbf{r}_B,\mathbf{r}_A,\omega)\, \hat{d}_A^j|^2}, \tag{3b}$$

where $\mathcal{G}^0(\mathbf{r}_B,\mathbf{r}_A,\omega)$ is the free-space Green's tensor, with a well-known analytical expression [47], and $\mathcal{G}(\mathbf{r}_B,\mathbf{r}_A,\omega)$ is the Green's tensor for the geometry under consideration. From the above expressions it is clear that calculating the Green's tensor for a geometry gives both the SE and ET rates in that geometry.

Following our previous work [43] and that of others [47] on the subject, the Green's tensor for any particular geometry, $\mathcal{G}(\mathbf{r},\mathbf{s},\omega)$, can be split into a *homogeneous* part, $\mathcal{G}_h(\mathbf{r},\mathbf{s},\omega)$, which is nonzero only when the two molecules are in the same medium (i.e., not separated by any surface of discontinuity in the dielectric properties of matter), and a *scattering* part, $\mathcal{G}_s(\mathbf{r},\mathbf{s},\omega)$, which accounts for the presence of such surfaces of discontinuity:

$$\mathcal{G}(\mathbf{r},\mathbf{s},\omega) = \mathcal{G}_h(\mathbf{r},\mathbf{s},\omega) + \mathcal{G}_s(\mathbf{r},\mathbf{s},\omega).$$

In Cartesian coordinates, the expression of the homogeneous part of the Green's tensor is well known [47]:

$$\begin{aligned}\mathcal{G}_h(\mathbf{r},\mathbf{s},\omega) = &-\frac{\delta(\mathbf{r}-\mathbf{s})}{k^2}\hat{\mathbf{z}}\hat{\mathbf{z}} + \frac{i}{8\pi^2}\int d^2k_\rho \frac{1}{k_z k_\rho^2} \\ &\times\{\mathbf{M}(\mathbf{k}_\rho, \pm k_z,\mathbf{r}) \otimes \mathbf{M}^*(\mathbf{k}_\rho, \pm k_z,\mathbf{s}) \\ &+\mathbf{N}(\mathbf{k}_\rho, \pm k_z,\mathbf{r}) \otimes \mathbf{N}^*(\mathbf{k}_\rho, \pm k_z,\mathbf{s})\} z \gtrless z_s,\end{aligned} \tag{4}$$

where $k = |\mathbf{k}| = |(\mathbf{k}_\rho, k_z)| = \omega\sqrt{\varepsilon(\omega)}$ is the wave number of light in the homogeneous medium, $\mathbf{k}_\rho$ is the component of the wave vector of light in the xy plane, and $k_z = \sqrt{k^2 - k_\rho^2}$ is the z component of this wave vector. The symbol $\otimes$ represents the tensor (or Kronecker) product of two vectors.

The *vector wave functions*, $\mathbf{M}$ and $\mathbf{N}$, also have well-known expressions [47]:

$$\mathbf{M}(\mathbf{k}_\rho, \pm k_z,\mathbf{r}) = i(\mathbf{k}_\rho \times \hat{\mathbf{z}})\, e^{i\mathbf{k}_\rho\cdot\boldsymbol{\rho}}\, e^{\pm i k_z z}, \tag{5a}$$

$$\mathbf{N}(\mathbf{k}_\rho, \pm k_z,\mathbf{r}) = -\frac{1}{k}\left(\pm k_z \mathbf{k}_\rho - k_\rho^2 \hat{\mathbf{z}}\right) e^{i\mathbf{k}_\rho\cdot\boldsymbol{\rho}}\, e^{\pm i k_z z}, \tag{5b}$$

where $\mathbf{M}$ corresponds to *transverse electric* (TE) modes, while $\mathbf{N}$ corresponds to *transverse magnetic* (TM) modes.

If we now consider an inhomogeneous medium, in which the dielectric properties vary in a piece-wise fashion in the z direction alone [i.e., $\varepsilon(\mathbf{r},\omega) = \varepsilon(z,\omega)$], we have a model for a planar multilayered geometry, of which the slab and the planar

waveguide are examples. The scattering part of the Green's tensor, $\mathcal{G}_s(\mathbf{r},\mathbf{s},\omega)$, in this geometry, has a form analogous to the homogeneous part [47]:

$$\mathcal{G}_s(\mathbf{r},\mathbf{s},\omega) = \frac{i}{8\pi^2}\int d^2k_\rho \frac{1}{k_z k_\rho^2}[R_M \mathbf{M}(\mathbf{k}_\rho, \pm k_z,\mathbf{r}) \otimes \mathbf{M}^*(\mathbf{k}_\rho, \pm k_z,\mathbf{s}) + R_N \mathbf{N}(\mathbf{k}_\rho, \pm k_z,\mathbf{r}) \otimes \mathbf{N}^*(\mathbf{k}_\rho, \pm k_z,\mathbf{s})], \quad (6)$$

with the coefficients R_M and R_N introduced to account for scattering from the various interfaces that make up the geometry. These coefficients can be calculated by imposing the appropriate continuity conditions on the components of the Green's tensor across the various interfaces. As this is a relatively straightforward procedure, the details of which can be found elsewhere [43,47], we shall not give it here. We shall return, instead, to the expressions given for the normalized SE and ET rates [Eq. (3)]. The normalized SE rate is seen to be linear in the Green's tensor, and so, splitting this tensor into a homogeneous and a scattering part allows us to make explicit the effect that the presence of surfaces of discontinuity has on the SE rate. We can now write

$$\tilde{\gamma}(\mathbf{r},\omega) = n(\omega) + \frac{6\pi}{k}\hat{d}_i \,\mathrm{Im}\big[\mathcal{G}_s^{ij}(\mathbf{r},\mathbf{r},\omega)\big]\,\hat{d}_j, \quad (7)$$

where a summation over the component indices i and j is implicitly understood and where $n(\omega)$ stands for the (real part of the) refractive index of the medium into which the molecule is embedded. In the present paper, the decaying molecule is always embedded in an inert medium, whose dielectric permittivity is a (real) constant. When the molecule is inside an absorbing medium, one must use the transverse part of the Green's tensor to calculate the radiative decay rate [48]. The linear dependence of the normalized SE rate on the Green's tensor also makes it straightforward to identify even further contributions (i.e., contributions coming from the several types of surface-plasmon polaritons which we shall introduce later on).

When we consider the normalized ET rate between two molecules, no such split is possible, since the normalized ET rate is quadratic in the Green's tensor and, therefore, interference effects between what can be called *direct interaction*, resulting from the homogeneous part of the Green's tensor, and *indirect interaction*, resulting from the scattering part, also contribute to the normalized ET rate. The contributions resulting from the different surface-plasmon polaritons are, correspondingly, somewhat more difficult to sort out.

We now return to considering the numerical implementation of calculating the Green's tensor and the SE and ET rates. The homogeneous part of the Green's tensor can be straightforwardly calculated in closed form [43], which leaves only the scattering part to be calculated numerically. Expression (6) can be further simplified by considering polar coordinates for the wave vector and performing the angular integral analytically. This is possible, since the geometry has a rotational symmetry around the z axis and the R coefficients in (6) depend only on the magnitude of the wave vector $\mathbf{k}_\rho$.

Without going through the detailed analytical calculations (the reader may wish to consult [47] and [49] for a more step-by-step account), we give below the expression for a particular component of the scattered part of the Green's tensor:

$$\mathcal{G}^{zz}_{s(ij)}(\mathbf{r},\mathbf{s},\omega) = \frac{i}{4\pi}\int_0^\infty dk_\rho \frac{k_\rho^3}{k_{zj}k_i k_j} R_N^{\pm(ij)\pm} e^{\pm i k_{zi} z} e^{\pm i k_{zj} z_s} \times J_0(k_\rho|\boldsymbol{\rho}-\boldsymbol{\rho}_s|), \quad (8)$$

where a summation is implied over the $\pm$ indices on the R coefficients. The left-side $\pm$ index accounts for the direction of propagation along the z axis of an electromagnetic mode at the acceptor's location, denoted by $\mathbf{r} = (\boldsymbol{\rho}, z)$, while the right-side $\pm$ index stands for the same propagation direction at the donor's location, denoted by $\mathbf{s} = (\boldsymbol{\rho}_s, z_s)$. The $\pm$ signs in the exponential functions have the same value as the corresponding indices on the R coefficients. Each electromagnetic mode in the above integral is identified by the in-plane component of its wave vector, k_ρ, and its polarization (in this case, purely TM modes, denoted by the subscript N on the R coefficients). The z component of the wave vector is given by $k_{zi} = \sqrt{k_i^2 - k_\rho^2} = \sqrt{\omega^2\varepsilon_i - k_\rho^2}$. Each mode, in turn, enters the above integral weighted by the R coefficients. This expression gives the zz component of the scattering part of the Green's tensor when the donor molecule is located at position $\mathbf{s} = (\boldsymbol{\rho}_s, z_s)$ in layer j and the acceptor molecule is located at position $\mathbf{r} = (\boldsymbol{\rho}, z)$ in layer i. J_0 is the Bessel function of first kind and zeroth order, which is the result of the integration over the angular variable. The remaining integral in (8) cannot be performed analytically, and we resort to numerical integration in the complex k_ρ plane using integration routines from the free-software GNU Scientific Library [50], adapted for our purposes. It is possible to numerically extract the contributions from different poles in the integrand of Eq. (8), and we perform that extraction for surface-plasmon polariton poles, thus separating their contribution (see [51] for the technical details of such a pole extraction).

B. Surface-plasmon polaritons on a single planar interface

In this section we consider the existence of *surface-plasmon polaritons* (SPPs) on a planar interface between a metal and a dielectric. We will consider a general model, but will also give relevant numerical values for the interface between silver (Ag) and silica (SiO_2), following the experimental data of Johnson and Christy [52]. SPPs are modes of the electromagnetic field that only propagate along the interface between two media (metal and dielectric), and decay exponentially away from this interface, on both sides. We consider one of the two half-spaces, occupying the region with $z < 0$, to consist of a metal of frequency-dependent dielectric permittivity $\varepsilon_m(\omega)$ given by a Drude model:

$$\varepsilon_m(\omega) = 1 - \frac{\omega_P^2}{\omega^2 + i\gamma\omega}, \quad (9)$$

and the other half-space, occupying the region with $z > 0$, to consist of a dielectric material with constant permittivity ε_d ($\varepsilon^{SiO_2} \approx 4.0$). In the above expression, ω_P is the plasma frequency of the metal ($\omega_P^{Ag} = 9.176$ eV), and γ is the linewidth responsible for losses in the metal ($\gamma^{Ag} = 0.021\,\mathrm{eV} = 2.288 \times 10^{-3}\,\omega_P^{Ag}$). For the purposes of introducing SPPs, we consider a lossless metal, setting $\gamma = 0$. Using

Maxwell's equations and the continuity conditions at the interface between the two media, one can derive the dispersion relations for the *transverse magnetic* (TM) modes supported by this structure [53], written as expressions for the components of the wave vector as

$$k_x = \omega\sqrt{\frac{\varepsilon_d\varepsilon_m}{\varepsilon_d+\varepsilon_m}}, \quad k_z^{d,m} = \omega\sqrt{\frac{\varepsilon_{d,m}^2}{\varepsilon_d+\varepsilon_m}}, \tag{10}$$

where k_x is the tangential component, continuous across the interface, and k_z^d and k_z^m are the normal components in the dielectric and metal, respectively. The rotational symmetry around the z axis permits us to set $k_y^d = k_y^m = 0$.

The conditions for the existence of SPPs can now be derived by requiring that k_z^d and k_z^m be purely imaginary (confinement to the interface), and k_x be purely real. Using expressions (10) for the wave vector components, and the fact that the permittivity of the dielectric material is real and positive, $\varepsilon_d > 0$, one finds that $\varepsilon_m \leqslant -\varepsilon_d$. Considering a Drude model with vanishing linewidth $\gamma = 0$, SPPs are restricted to a frequency interval of $0 \leqslant \omega \leqslant \omega_{\rm SP}$, where $\omega_{\rm SP}$ is the *surface-plasmon frequency* given by

$$\omega_{\rm SP} = \sqrt{\frac{\omega_P^2}{1+\varepsilon_d}}. \tag{11}$$

For the Ag/SiO_2 interface, the surface-plasmon frequency is $\omega_{\rm SP}^{\rm Ag/SiO_2} = 4.103\,{\rm eV} = 0.447\,\omega_P^{\rm Ag/SiO_2}$.

The dispersion relation $\omega(k_x)$ is shown schematically in Fig. 1 (see also [53]) for a lossless Drude metal and a dielectric with $\epsilon_d = 4$.

In addition to the SPP region, $0 \leqslant \omega \leqslant \omega_{\rm SP}$, there also exists a *stop gap* for $\omega_{\rm SP} < \omega < \omega_P$, where no propagating modes exist. In the *radiative region* above the plasma frequency, all the modes can propagate freely in both the metal and the dielectric.

Although we have only considered a lossless Drude model with $\gamma = 0$ thus far, this limitation is not very severe in practice. The effect of a nonzero γ is to introduce a small imaginary component k_x'' for the wave vector, which leads to dampening

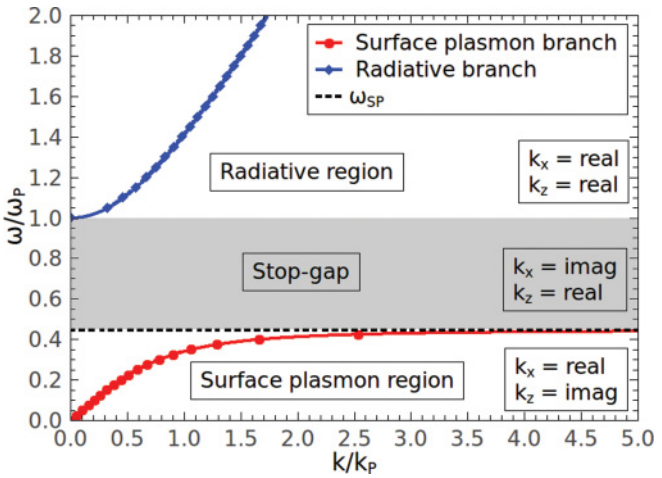

FIG. 1. (Color online) Dispersion relation of SPPs at the interface between a dielectric with $\epsilon_d = 4$ and a lossless Drude metal. k_P is the wave number corresponding to the plasma frequency.

of the SPPs as they propagate along the interface. For the Ag/SiO_2 system at $\omega = 0.40\,\omega_P$, close to the surface-plasmon frequency $\omega_{\rm SP} = 0.447\,\omega_P$, the propagation length L of an SPP, defined as $L = 1/k_x''$ such that $|e^{ik_xL}| = 1/e$, is rather large, $L \approx 56\,\lambda_P^{\rm Ag} \approx 7.56\,\mu$m, for $\gamma = 2.288 \times 10^{-3}\,\omega_P$, the linewidth of Ag at optical frequencies.

One of the most interesting features of SPPs is their behavior near the surface-plasmon frequency $\omega_{\rm SP}$. From Fig. 1 one can see that, as the frequency approaches $\omega_{\rm SP}$, the propagation constant along the interface, k_x, increases enormously—in the lossless limit $k_x \to \infty$. Therefore, at frequencies close to $\omega_{\rm SP}$, which can lie in the optical region, the wavelength $\lambda \propto k_x^{-1}$ becomes very small, possibly in the x-ray region. As it is near the surface-plasmon frequency $\omega_{\rm SP}$ that the effect of SPPs is greater, in the rest of the paper we shall mostly focus on this frequency region (i.e., $\omega = 0.40\,\omega_P$).

III. METALLIC SLAB

In this section we consider a Drude metallic slab of thickness d and dielectric permittivity $\varepsilon_m(\omega)$ given by Eq. (9) embedded in a dielectric material with constant dielectric permittivity $\varepsilon_d = 4$. This geometry is presented schematically in Fig. 2. We have calculated both the SE rate of a molecule and the ET rate between two molecules placed near the slab, focusing on the role that SPPs have in modifying these rates.

In calculating the dispersion relations for this geometry, the mirror symmetry plane at $z = 0$ leads to two different types of SPPs with the following dispersion relations [54,55]:

$$\varepsilon_m k_z^d + \varepsilon_d k_z^m \tanh\left(-ik_z^m d/2\right) = 0, \tag{12a}$$

$$\varepsilon_m k_z^d + \varepsilon_d k_z^m \coth\left(-ik_z^m d/2\right) = 0. \tag{12b}$$

The two different types are the antisymmetric branch [Eq. (12a)] and symmetric branch [Eq. (12b)], with respect to the mirror symmetry plane at $z = 0$. The dispersion relations for the SPPs are shown graphically in Fig. 3 for two different slab thicknesses, $d = 0.01\,\lambda_P$ and $d = 0.20\,\lambda_P$, where λ_P is the wavelength associated with the plasma frequency ω_P of the Drude metal slab. The plasma frequency of Ag is $\omega_P^{\rm Ag} = 9.176$ eV, corresponding to a wavelength of $\lambda_P^{\rm Ag} = 135.12$ nm [52]. The two corresponding slab thicknesses are, therefore, $d = 0.01\,\lambda_P^{\rm Ag} = 1.35$ nm and $d = 0.20\,\lambda_P^{\rm Ag} = 27.02$ nm. In this geometry, the symmetric branch of the SPP exists partially in the stop gap between $\omega_{\rm SP}$ and ω_P, where no modes exist on a single interface between a metal and a dielectric (see Fig. 1). This happens, however, only when the thickness of the metallic slab is small enough so that the SPP dispersion relation splits into two branches [Eq. (12)]. When

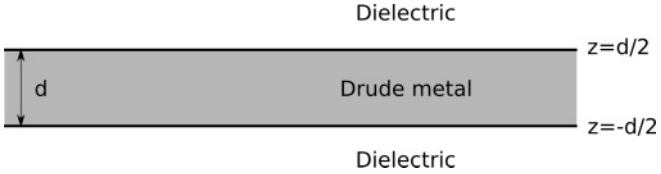

FIG. 2. Geometry of a Drude metal slab of thickness d embedded in a dielectric material.

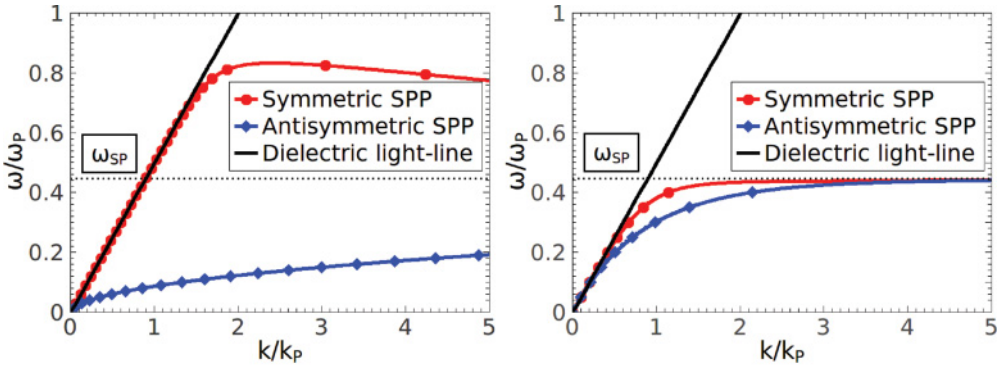

FIG. 3. (Color online) Dispersion relations for SPPs in a slab geometry.

$-i\,k_z^m\,d/2 \gtrsim 2.0$, or $d \gtrsim 4.0\,\delta_m$, where $\delta_m = 1/\mathrm{Im}(k_z^m)$ is the penetration depth of the SPPs inside the Drude metal slab, then $\tanh(-ik_z^m d/2) \approx \coth(-ik_z^m d/2) \approx 1$ and the two distinct SPP dispersion relations reduce to the dispersion relation for SPPs on a planar interface between a metal and a dielectric half-space [Eq. (10)]. For a Ag slab embedded in SiO_2, the SPP frequency is $\omega_{\mathrm{SP}}^{\mathrm{Ag}} \approx 4.103$ eV, with a corresponding wavelength of $\lambda_{\mathrm{SP}}^{\mathrm{Ag}} = 302.13$ nm. Close to this frequency, namely at $\omega = 0.40\,\omega_P^{\mathrm{Ag}} = 3.67$ eV, the penetration depth of SPPs inside silver is $\delta^{\mathrm{Ag}} = 1/\mathrm{Im}(k_z^{\mathrm{Ag}}) \approx 80$ nm. When the slab thickness is larger than this penetration depth, the SPPs on the two interfaces of the slab decouple, and each SPP is localized at a single interface.

In the next subsection we calculate the SE rate of a molecule placed above a Drude slab and investigate the effect of SPPs on the rate.

A. Spontaneous emission

We first consider a molecule with a molecular transition dipole along the z axis and placed above a Drude metal slab of thickness d, embedded in a dielectric medium with constant dielectric permittivity, $\varepsilon_d = 4$. Figure 4 presents the various decay rates of the molecule for several slab thicknesses as a function of both distance to the slab and frequency. Figures 4(a) and 4(d) show, in a logarithmic scale, a contour plot of the total emission rate of the molecule as a function of both frequency ω and distance z to the slab, for two slab thicknesses, $d = 0.01\,\lambda_P$ and $d = 0.20\,\lambda_P$. Figures 4(b) and 4(e) show the distance dependence of the different contributions to the emission rate at a frequency close to the surface-plasmon frequency, $\omega = 0.40\,\omega_P$, or $\omega_{\mathrm{Ag}} = 3.67$ eV ($\lambda_{\mathrm{Ag}} = 337.8$ nm) in a Ag/SiO_2 environment, and for the same two slab thicknesses. The contributions of the two types of SPPs, symmetric and antisymmetric, are clearly shown, as is the radiative emission rate (i.e., the emission into photons freely propagating in the dielectric medium). A further contribution to the decay rate of the molecule, via the *lossy surface waves* (LSW), is also present at very small distances from the surface of the slab. This contribution, which, unlike SPPs, is completely absent in the case of a lossless Drude metal, comes about because of the presence of losses in the metal and it is related to excitation of electron-hole pairs [56].

Finally, Figs. 4(c) and 4(f) show the frequency dependence of the total emission rate of a molecule at different distances from a slab of the same two thicknesses as in the previous four panels. The frequency range spans the interval $\omega \in (0,\omega_P)$, encompassing both what in Figs. 4(a) and 4(d) we have called the *surface-plasmon region*, where SPPs can be excited, and the *stop gap*, where no SPPs exist on a single interface.

In Figs. 4(a) and 4(d) it is evident that the largest enhancement of the emission rate occurs very close to the interface and very close to the surface-plasmon frequency, ω_{SP}, although for the case of the thinner slab in Fig. 4(a), the enhancement is still appreciable even at relatively larger distances from the slab and at frequencies far from ω_{SP}. We shall discuss this effect further when we analyze Figs. 4(c) and 4(f).

Figures 4(b) and 4(e) break down the emission rate at $\omega = 0.40\,\omega_P$ into individual contributions coming from the radiative emission rate, as well as the SPPs. As one would expect by considering the dispersion curves for SPPs from Fig. 3, as the slab thickness increases, the two contributions from the two types of SPPs become more and more similar to one another and to the contribution of an SPP on a single interface between a dielectric and a metal. For smaller slab thicknesses [Fig. 4(b)], there is a marked difference between the two contributions. At the frequency that we use, $\omega = 0.40\,\omega_P$ ($\omega = 3.67$ eV and $\lambda = 337.8$ nm for Ag/SiO_2), the antisymmetric SPP has a very large parallel component of the wave vector and hence, a very small penetration depth inside both the dielectric and the Drude slab. Its contribution to the decay rate is, therefore, significant only when the molecule is very close to the slab (below 5 nm for the Ag/SiO_2 geometry). The symmetric SPP, on the other hand, has its dispersion curve very close to the light line in the dielectric [Fig. 3(a)] and the SPP is, therefore, weakly confined to the interface, contributing significantly to the decay rate even when the molecule is several wavelengths distant from the slab. In all cases, the total decay rate of the molecule at sufficiently large distances from the slab reverts to its value in a homogeneous medium of dielectric permittivity $\varepsilon_d = 4$. The difference between the curves representing the total decay rate, and the sum of the contributions from the radiative decay rate and the SPP decay rates comes from the LSW contribution, which, as we mentioned previously, is absent for a lossless

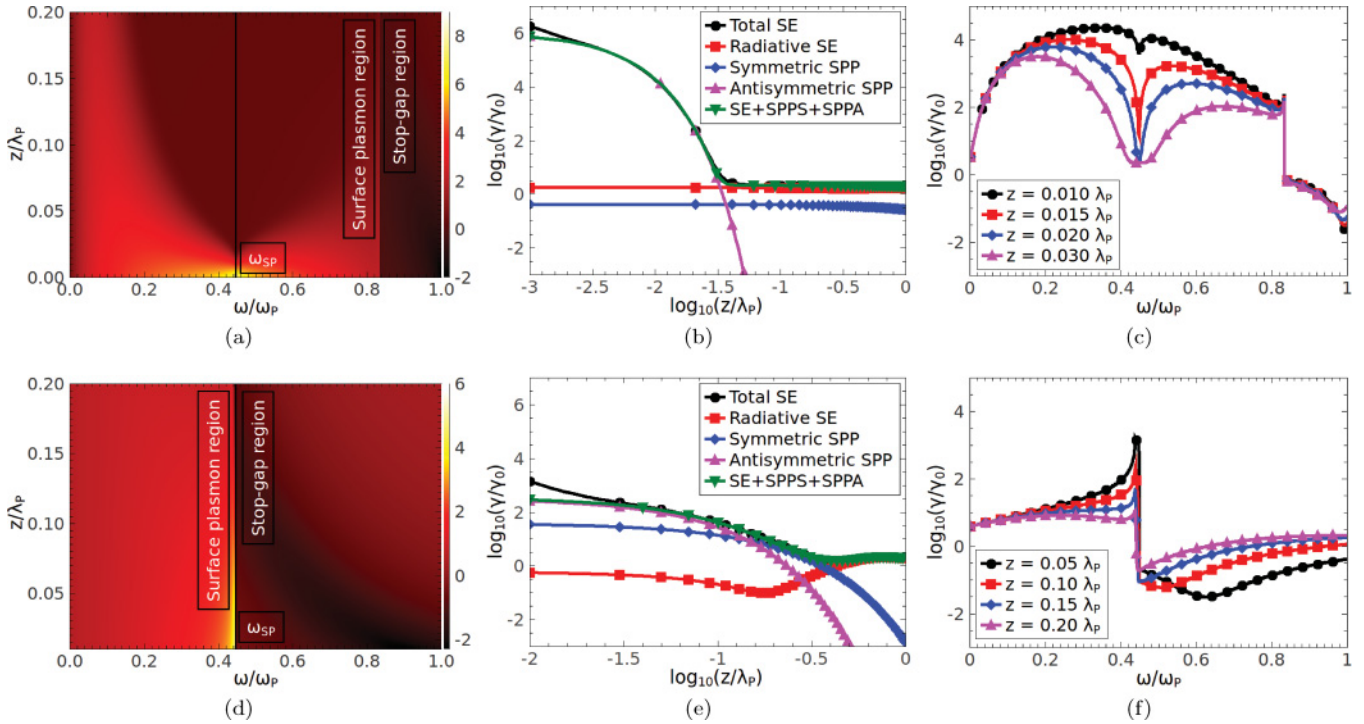

FIG. 4. (Color online) Relative decay rates of a molecule above a Drude slab with $\gamma = 2.288 \times 10^{-3}\,\omega_P$. The thickness of the slab is $d = 0.01\,\lambda_P$ for the three panels on the top row and $d = 0.20\,\lambda_P$ for the three panels on the bottom row. This corresponds, in a Ag/SiO_2 environment, to $d = 1.36$ nm and $d = 27.02$ nm, respectively. (a) and (d) The decay rates as a function of both frequency and distance to the upper surface of the slab; (b) and (e) the different contributions to the relative decay rate as a function of distance to the slab at a frequency $\omega = 0.40\,\omega_P$; (c) and (f) the frequency dependence of the relative decay rate for several molecule-slab separations.

Drude metal. The LSW contribution is significant only when the molecule is very close to the surface of the slab, and it is more marked for the thicker slab [Fig. 4(e)].

The last two panels, Figs. 4(c) and 4(f), depict the frequency dependence of the total emission rate of a molecule at several distances above a slab of thickness $d = 0.01\,\lambda_P$ [Fig. 4(c)] and $d = 0.20\,\lambda_P$ [Fig. 4(f)]. For the smaller of the two thicknesses [Fig. 4(c)], the frequency range where SPPs can be excited is larger, as seen from the dispersion curves in Fig. 3(a). Correspondingly, there is an increase in the emission rate of the molecule in this frequency range. Two peaks in the emission rate are clearly present. At small molecule-slab separations, the near field of the molecule can successfully excite SPPs of very large wave vectors, whose frequency lies very close to the surface-plasmon frequency ω_{SP}. As this separation is increased, the near field of the molecule, due to its evanescent nature, can only couple to wave vectors with smaller in-plane components, and thus can excite SPPs with a smaller wave vector, and frequency further away from ω_{SP}. The peak of the emission rate is then shifted away from the surface-plasmon frequency, toward lower frequencies (antisymmetric SPP) and higher frequencies (symmetric SPP). As the frequency grows larger and exits the region where SPPs can be excited, the emission rate drops abruptly and is essentially equal to the radiative emission rate.

For the larger of the two slab thicknesses, $d = 0.20\,\lambda_P$, no SPPs can be excited above the surface-plasmon frequency ω_{SP} [see also Fig. 3(b)] and the surface-plasmon frequency region is delimited by ω_{SP}, as illustrated in Fig. 4(d) as well. As the molecule-slab separation is increased, the shift of the peak in the emission rate occurs only toward lower frequencies, and above ω_{SP}, the emission rate is again basically equal to the radiative emission rate.

B. Energy transfer

We turn now to calculating the ET rate between two molecules placed near a Drude metal slab. Figure 5 shows the two configurations of molecules that we use in calculating the ET rate. The fact that SPPs can be excited at the two surfaces of the slab has interesting consequences. For the first configuration in Fig. 5, one can calculate the ET through the slab, and investigate how the excitation of SPPs influences this transfer. As was mentioned before, for small slab thicknesses both symmetric and antisymmetric SPPs can be excited; their electromagnetic field extends between the two surfaces of the slab, thus being able to facilitate the energy transfer between molecules placed on opposite sides of the slab.

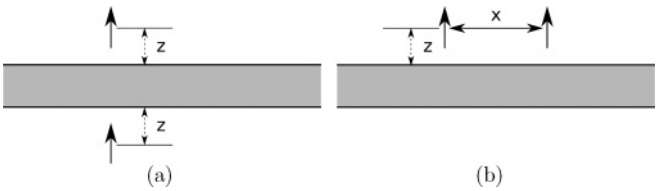

FIG. 5. Two configurations of molecules used in calculating the ET rate in the presence of the Drude metallic slab.

Figure 6 shows the ET rate for slabs of different thicknesses, when the two molecules are in the two configurations of Fig. 5. Figure 6(a) shows the ET rate through the slab for the configuration in Fig. 5(a). The molecules are placed on the same z axis, and their dipole moments are oriented along z as well. For all the curves in this figure, the relative ET rate drops off monoexponentially at small values of z, with a decay distance roughly equal to the characteristic decay distance of the antisymmetric SPP. This suggests that transfer of energy occurs predominantly through the antisymmetric SPP. For thicknesses even larger than shown in Fig. 6(a), the ET rate through the slab is negligible, since the two extended SPPs become localized at each interface, failing to reach across the slab.

Figure 6(b) shows the ET rate along the slab, for the configuration in Fig. 5(b). The molecules are placed on the same side of the slab, at a distance of $z = 0.01\,\lambda_P = 1.35$ nm from its surface, and with their dipole moments oriented along the z axis. The ET rate is plotted as a function of the x distance between the molecules in the plane of the slab. If the molecules are placed on the same side of the slab, one can investigate how the excitation of the two different types of SPPs influences the transfer of energy along the metal slab. Depending on the thickness of the slab, d, the symmetric and antisymmetric SPPs can have very different propagation lengths along the surface of the slab, just as their penetration depth inside the slab can be markedly different, especially near the surface-plasmon frequency ω_{SP} (see also the discussion in the previous subsection).

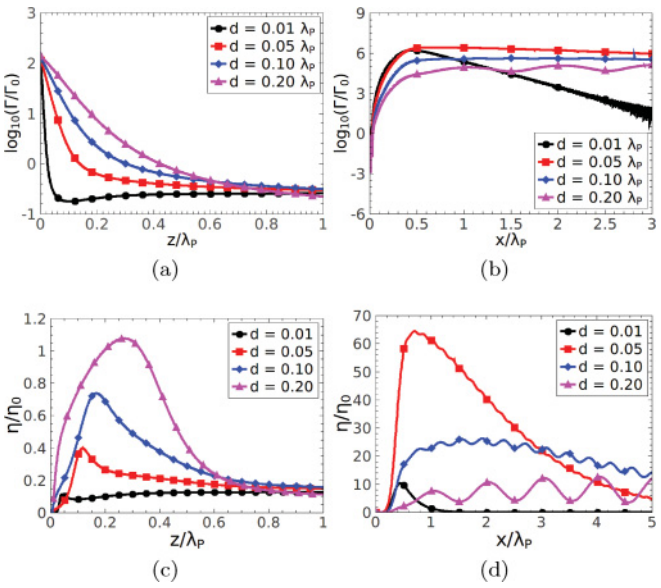

FIG. 6. (Color online) (a) Relative ET rate between two molecules in the configuration from Fig. 5(a), with the ET rate plotted as a function of the distance z between a molecule and its corresponding surface of the slab; (b) relative ET rate for the configuration from Fig. 5(b), with the ET rate plotted as a function of the distance x between the molecules, when the molecules are at a distance $z = 0.01\,\lambda_P$ from the upper surface of the slab; (c) $\tilde{\eta}$ ratio for the configuration from Fig. 5(a); (d) $\tilde{\eta}$ ratio for the configuration from Fig. 5(b). The frequency is $\omega = 0.40\,\omega_P$, the linewidth is $\gamma = 2.288 \times 10^{-3}\,\omega_P$.

If we consider the x dependence of the SPPs, in addition to the dampening due to ohmic losses in the metal slab, there also exists a (much larger for the linewidth γ considered here) dampening due to the circular symmetry of the geometry. The SPPs are excited by a point dipole and, therefore, they propagate along the interface from a single point, leading to this dampening. The symmetric SPP, whose wave vector is the smaller of the two, has a long characteristic wavelength, while the characteristic wavelength of the antisymmetric SPP is shorter. This mismatch in wavelength between the SPPs, coupled to the fact that the ET rate from Eq. (3b) depends on the square of the Green's tensor, and therefore includes interference terms between different contributions to this tensor, accounts for the oscillations visible in the curves in Fig. 6(b). For the thicker slabs ($d = 0.10\,\lambda_P$ and $d = 0.20\,\lambda_P$), the characteristic wavelengths of the two SPPs at $\omega = 0.40\,\omega_P$ are comparable in magnitude, while still differing. The amplitude of the two contributions is also comparable, which leads to pronounced interference effects between them and a clearly discernible oscillatory behavior of the relative ET rate. For the thinner slabs ($d = 0.01\,\lambda_P$ and $d = 0.05\,\lambda_P$), the dispersion curves of the two SPPs differ dramatically from each other. The characteristic wavelengths of the SPPs at $\omega = 0.40\,\omega_P$ are, therefore, also markedly different, as are their individual contributions to the ET rate. The interference effects are still present, but much weaker, and the main contribution to the ET rate comes, in this case, from the short-wavelength antisymmetric SPP, as the less pronounced oscillations modulating the ET rate curves in Fig. 6(b) illustrate.

In addition to considering the SE and ET rates relative to their values in free space, another useful comparison is between the SE and ET rates themselves, in the same geometry. The reason is that the energy-transfer rate can only be measured if it is comparable to or larger than the decay rate of the donor due to other channels. Assuming that the decay of the donor due to vibrational interactions is small (so that the donor's quantum yield in vacuum is large), we compare the ET rate to the SE rate, which includes decay due to all electromagnetic interactions (i.e., also due to SPPs). Thus, we define $\eta \equiv \Gamma/\gamma$; if $\eta > 1$, ET is the dominant channel for the donor to lose its energy. In Figs. 6(c) and 6(d), we plot the ratio,

$$\tilde{\eta} \equiv \frac{\eta}{\eta_0} = \frac{\Gamma/\gamma}{\Gamma_0/\gamma_0} = \tilde{\Gamma}/\tilde{\gamma}, \tag{13}$$

corresponding to the situation of Figs. 6(a) and 6(b), respectively. Thus, these plots show the role of the geometry (and implicitly SPPs) in favoring one decay channel of the donor (excitation transfer to the acceptor) over another (spontaneous decay), when compared to free space. From Fig. 6(c) we observe that for the molecular configuration of Fig. 5(a) for almost all slab thicknesses, the ratio $\tilde{\eta}$ is smaller than unity, expressing the fact that the enhancement of the ET rate in the presence of the metal slab is smaller than the enhancement of the SE rate in the presence of the metal slab. Consequently, it may be difficult to experimentally observe the energy transfer in this particular geometry.

The situation is quite different for the molecular configuration from Fig. 5(b). For this case, we observe that the ratio $\tilde{\eta}$ can be much greater than unity, which means that the effect of the

metal slab may strongly favor energy transfer from the donor to the acceptor over the spontaneous decay of the donor. We note that, since in the geometry of Fig. 5(b) the SE rate does not depend on x, the curves in Fig. 6(d) are just scaled versions of those in Fig. 6(b) (now plotted in a linear scale); the same does not hold for Figs. 6(c) and 6(a), in which corresponding curves really are functionally different from each other, because the SE rate depends on z.

The results presented in Fig. 6 have been obtained when both the donor and acceptor are oriented along the z direction, perpendicular to the metal slab. It is straightforward to generalize them for different orientations of the molecules as well as for rotational averages.

IV. PLANAR WAVEGUIDE

This section is dedicated to investigating the role of SPPs in the electromagnetic interactions of molecules (i.e., spontaneous emission and energy transfer) placed inside a planar waveguide. The planar waveguide is shown in Fig. 7 and it consists of a dielectric slab with permittivity $\varepsilon_2 = 4$ and thickness d_2 sandwiched between two Drude metal slabs of thickness d_1. Analogous to the case of the single Drude slab, the symmetry plane at $z = 0$ for this geometry splits the dispersion relation of the SPP of this geometry into four distinct branches: two groups of symmetric and antisymmetric SPPs, associated with the two types of interfaces comprising the geometry, an external interface between the Drude slab and the vacuum outside the waveguide, and an internal interface between the Drude slab and the material comprising the interior of the waveguide [57,58]. These dispersion diagrams are shown in Fig. 8 for several parameters of the waveguide. The four different branches of the dispersion relation are as follows: external antisymmetric SPP (EASPP), external symmetric SPP (ESSPP), internal antisymmetric SPP (IASPP), and internal symmetric SPP (ISSPP).

A. Spontaneous emission rate

In this subsection we present calculations of the emission rates of molecules placed in the vicinity of a waveguide, emphasizing the contribution of SPPs to these rates. Figure 9 shows the total SE rate of a molecule placed above the waveguide of Fig. 7, as well as the radiative emission rate and the emission rate into the different types of SPPs mentioned in the beginning of this section. The log-log scale employed here makes these different contributions to the SE rate plainly

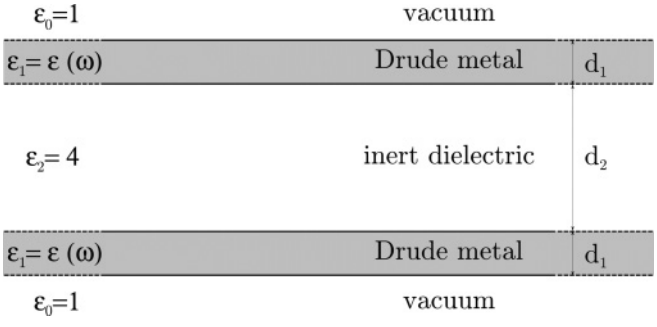

FIG. 7. Geometry of the waveguide.

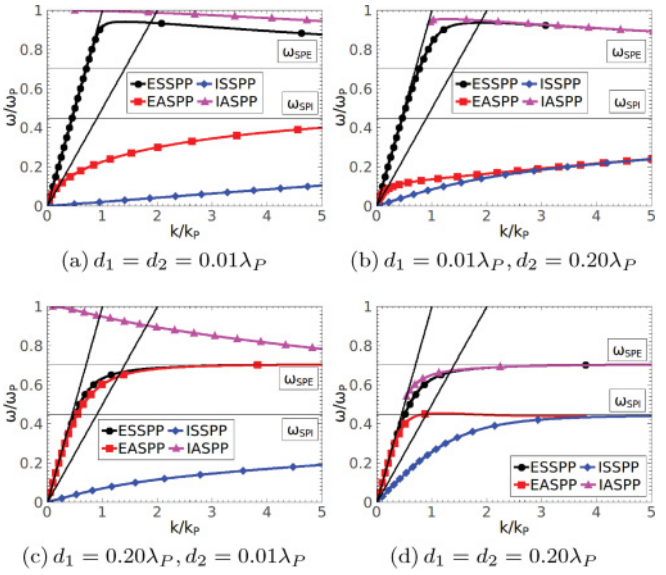

FIG. 8. (Color online) Dispersion relations for SPPs in a waveguide geometry with $\gamma = 0$.

visible. The frequency used for these calculations is $\omega = 0.40\,\omega_P$, close to the *internal surface-plasmon frequency*, $\omega_{\mathrm{SPI}} = 1/\sqrt{5}\,\omega_P \approx 0.447\,\omega_P$.

Figure 9(a) corresponds to thicknesses $d_1 = d_2 = 0.01\,\lambda_P$, for which there is the maximum difference in the contributions of the different types of SPPs (see Fig. 8). The ESSPP, lying closest to the light line in vacuum, has the smallest contribution to the decay rate. The main contribution to the decay rate of the molecule comes from the EASPP, which, though more confined to the external surface of the waveguide than the ESSPP, couples much stronger to the molecule. Finally, the ISSPP, with its larger parallel component of the wave vector,

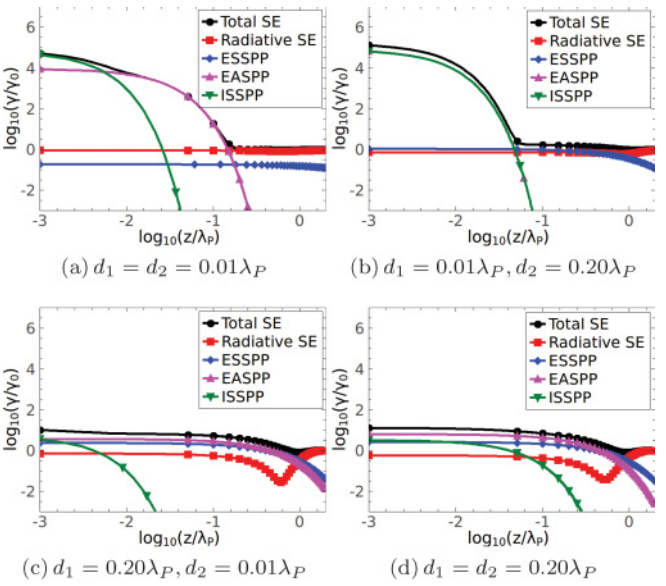

FIG. 9. (Color online) Relative decay rates of molecules above a planar waveguide, as a function of the distance to the surface of the waveguide, for $\gamma = 0$. The frequency is $\omega = 0.40\,\omega_P$, where no IASPP can be excited (see Fig. 8).

is the strongest confined to an interface, and its contribution is relevant only very close to the surface of the waveguide.

If we now increase the thickness of the material inside the waveguide, making $d_2 = 0.20\,\lambda_P$ [see Fig. 9(b)], the EASPP and ISSPP become virtually indistinguishable [see Fig. 8(b)], and their contributions to the decay rate are the same and constitute the dominant channels through which the molecule decays.

If, on the other hand, the thickness of the metal slabs is increased to $d_1 = 0.20\,\lambda_P$, while keeping the dielectric material inside the waveguide to a thickness of $d_2 = 0.01\,\lambda_P$ [see Fig. 9(c)], it is the ESSSP and EASPP that start to coincide [see Fig. 8(c)] and, hence, it is their contribution that is dominant and roughly the same, while the ISSPP contribution, though comparable to the others at very short distances from the waveguide, falls off abruptly as this distance increases.

Finally, when both thicknesses involved in the problem are set to $d_1 = d_2 = 0.20\,\lambda_P$, all types of SPPs have a relatively small parallel component of the wave vector [see Fig. 8(d)] and, hence, larger penetration depths in the materials [see Fig. 9(d)]. It is worth pointing out that in the last two panels in Fig. 9, where $d_1 = 0.20\,\lambda_P$, the enhancement of the decay rate is much smaller than in the first two panels, where $d_1 = 0.01\,\lambda_P$.

For all the panels in Fig. 9, the frequency used, $\omega = 0.40\,\omega_P$, forbids excitation of the IASPP, whose dispersion branch, Fig. 8 shows, lies completely above the internal SPP frequency ω_{SPI}.

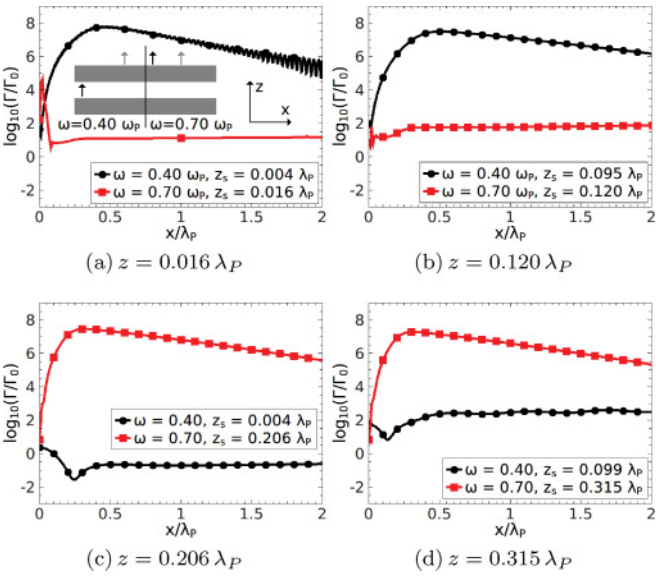

FIG. 10. (Color online) Relative ET rates between molecules in a planar waveguide geometry, as a function of their mutual separation along the x axis, for $\gamma = 2.288 \times 10^{-3}$. In the inset, which is the same for all four subfigures, the black arrow represents the donor molecule, fixed at z_s and $x_s = 0$, the gray arrow represents the acceptor molecule, fixed at z and with varying x position: (a) $d_1 = 0.01\,\lambda_P$, $d_2 = 0.01\,\lambda_P$; (b) $d_1 = 0.01\,\lambda_P$, $d_2 = 0.20\,\lambda_P$; (c) $d_1 = 0.20\,\lambda_P$, $d_2 = 0.01\,\lambda_P$; (d) $d_1 = 0.20\,\lambda_P$, $d_2 = 0.20\,\lambda_P$.

B. Energy transfer rate

This subsection is dedicated to investigating the ET rate between two molecules when placed inside and around the planar waveguide. Figure 10 shows the relative ET rate between the two molecules (donor and acceptor) as a function of their separation along the waveguide, for several z positions of the donor and acceptor, and two frequencies close to the two surface-plasmon frequencies associated with the structure, $\omega_{\mathrm{SPI}} = 1/\sqrt{5}\,\omega_P \approx 0.447\,\omega_P$ and $\omega_{\mathrm{SPE}} = 1/\sqrt{2}\,\omega_P \approx 0.707\,\omega_P$. One can thus investigate the transfer of excitation energy within the waveguide, as well as to the outside medium. The calculations are performed when both molecules have their transition dipole moments perpendicular to the plane of the waveguide, or along the z axis, and the two frequencies considered are $\omega = 0.40\,\omega_P$ and $\omega = 0.70\,\omega_P$. In a $Ag/SiO_2/Ag$ waveguide these correspond to wavelengths of $\lambda = 337.8$ nm and $\lambda = 193$ nm. The calculations in Fig. 10 have been performed for several thicknesses of the metallic plates and heights of the dielectric interior of the waveguide. In Fig. 10(a), the relevant parameters are $d_1 = d_2 = 0.01\,\lambda_P$. A large enhancement of the ET rate occurs from the inner to the outer surface of the metal plate, caused by excitation of the ISSPP by the near field of the donor located at $(x_s = 0, z_s = 0.004\,\lambda_P)$. The acceptor molecule couples to this SPP with its near field, resulting in a large enhancement of the ET rate. The fact that the maximum of the relative ET rate occurs when the intermolecular separation along the waveguide x is approximately $x \approx 0.5\,\lambda_P$ can be accounted for by the fact that what is plotted in Fig. 10 is the *normalized* ET rate (i.e., the ET rate in the planar waveguide normalized to its value in free space). When the intermolecular separation is very small, the ET rate is in its Förster regime and, inside the waveguide, is dominated by the direct interaction between the molecules (i.e., the energy transfer occurs mainly through exchange of virtual photons which do not scatter of the waveguide surfaces). As the intermolecular distance increases, the direct interaction contributes less, and the main contribution comes from the ISSPP. The rapid oscillations in the ET rate can be attributed, as in the case of a single metal plate, to interference between the different pathways of ET. In this case, it is the interference between the ISSPP and the EASPP which leads to these oscillations. At the frequency which is used, $\omega = 0.40\,\omega_P$, the dispersion curves of these two SPPs show the largest wave vector [see Fig. 8(a)], with the ISSPP wave vector the largest of the two. By contrast, when both molecules are placed outside the waveguide, and the frequency is close to the external plasmon frequency (i.e., $\omega = 0.70\,\omega_P$), there is almost no enhancement of the ET rate. At this particular frequency the EASPP dispersion curve is very close to the light line and no other SPPs are excited [see Fig. 8(a) again].

As the height of the dielectric interior of the waveguide is increased, the transfer rate from the inner to the outer surface of the metal plate is seen not to depend strongly on the height of the waveguide interior [see Fig. 10(b), the curve for $\omega = 0.40\,\omega_P$]. It is noticeable, however, that the oscillations in the ET rate are no longer present. The reason for this is that for this particular height of the waveguide interior, $d_2 = 0.20\,\lambda_P$, the ISSPP and EASPP dispersion curves nearly overlap [see Fig. 8(b)]. As such, the interference between these two pathways of energy transfer is always constructive, which leads to the absence of oscillations in the ET rate. Near the

external plasmon frequency, at $\omega = 0.70\,\omega_P$, the enhancement of the ET rate is much smaller, for the same reason as discussed in the above paragraph.

If, on the other hand, it is the thickness of the metal plate that is increased, as in Fig. 10(c), transfer from the interior to the exterior of the metal plate is actually suppressed near the internal plasmon frequency, $\omega = 0.40\,\omega_P$. In this case, even though the ISSPP still has a large wave vector, the acceptor molecule located on the outside of the waveguide can no longer couple to it efficiently. The EASPP, on the other hand, although capable of coupling to the donor molecule, has a wave vector very close to the light line and, hence, a very small contribution. Near the external plasmon frequency, at $\omega = 0.70\,\omega_P$, however, the wave vectors corresponding to both the EASPP and the ESSPP are much larger—they nearly coincide—and the ET transfer between two molecules close to the outer surface of the metal plates is considerably enhanced.

When both the thickness of the metal plates and the height of the waveguide interior are rather large [see Fig. 10(d)], there is a slight enhancement of the ET rate to the outside of the waveguide. On top of this enhancement there is a slight oscillation of the ET rate, due to interference between the IASPP and the ESSPP [see Fig. 8(d)] which, at $\omega = 0.40\,\lambda_P$, have wave vectors of the same order of magnitude. As in the previous case, the largest enhancement of the ET rate occurs when both molecules are close to the outer surface of the metal plate, mediated by the ESSPP at $\omega = 0.70\,\omega_P$.

Finally, we have also calculated the $\tilde{\eta}$ ratio from Eq. (13) for Fig. 10 and have observed effects similar to those discussed for Fig. 6. Since the position of the donor is kept fixed, the curves obtained have the same shape as those of Fig. 10, only scaled by the relative SE rate of the donor, and for this reason we do not present them here.

V. SUMMARY AND CONCLUSIONS

In this paper we have investigated the role that SPPs play in modifying the electromagnetic properties of atoms and molecules placed near a metallic slab embedded in a dielectric host, and in a planar waveguide. In these and other multilayered geometries, the presence of multiple interfaces gives rise to several branches in the dispersion relations of SPPs. These branches can be distinguished by their symmetries and their influence on the spontaneous emission rate and the energy-transfer rate has been investigated.

In a slab geometry, the dispersion relation of surface plasmons splits into two branches: symmetric and antisymmetric, which differ markedly from one another when the thickness of the slab is suitably small. Their influence on the SE and ET rates can, consequently, also differ appreciably, and we have been able to investigate this influence and relate it to specific properties of the SPPs (i.e., wavelength and frequency). It is close to the surface-plasmon frequency of the slab geometry ω_{SP} that the effect of the SPPs on the SE and ET rates is the strongest. At these frequencies, the wavelength of the SPPs (the antisymmetric SPP, to be precise) can be much smaller than that of light of the same frequency, which leads to subwavelength effects in the behavior of the SE and ET rates, such as very fast oscillations in the ET rate, for example.

If we consider the geometry of the planar waveguide, the SPP dispersion relation now splits into four branches: external symmetric and antisymmetric and internal symmetric and antisymmetric, with two surface-plasmon frequencies, associated with the external ω_{SPE} and internal ω_{SPI} SPPs. Depending on the positioning of molecules inside or around the planar waveguide, and on the molecule's characteristic frequency, they can be made to selectively couple to one or more of these SPPs and their spontaneous emission or energy-transfer rates can be dramatically modified. We have been able to identify the SPP branches that affect these rates the most for several particular parameters of the geometry and configurations of molecules.

This intricate dependence of the electromagnetic properties of molecules on geometrical parameters and frequency extends the space of possibilities for tailoring these properties.

ACKNOWLEDGMENT

This work was supported by NanoNed, a national nanotechnology program coordinated by the Dutch Ministry of Economic Affairs.

[1] E. M. Purcell, Phys. Rev. **69**, 681 (1946).
[2] K. Drexhage, J. Lumin. **1-2**, 693 (1970).
[3] H. Morawitz, Phys. Rev. **187**, 1792 (1969).
[4] F. Le Kien and K. Hakuta, Phys. Rev. A **75**, 013423 (2007).
[5] R. Matloob, Phys. Rev. A **62**, 022113 (2000).
[6] P. W. Milonni, Opt. Commun. **9**, 119 (1973).
[7] P. Stehle, Phys. Rev. A **2**, 102 (1970).
[8] D. T. Alves, C. Farina, and A. C. Tort, Phys. Rev. A **61**, 034102 (2000).
[9] M. R. Philpott, Chem. Phys. Lett. **19**, 435 (1973).
[10] H. Rigneault and S. Monneret, Phys. Rev. A **54**, 2356 (1996).
[11] C. E. Reed, J. Giergiel, J. C. Hemminger, and S. Ushioda, Phys. Rev. B **36**, 4990 (1987).
[12] T. Søndergaard and B. Tromborg, Phys. Rev. A **64**, 033812 (2001).
[13] D. P. Fussell, R. C. McPhedran, and C. Martijn de Sterke, Phys. Rev. A **71**, 013815 (2005).
[14] W. Żakowicz and M. Janowicz, Phys. Rev. A **62**, 013820 (2000).
[15] V. V. Klimov and M. Ducloy, Phys. Rev. A **69**, 013812 (2004).
[16] H. Chew, J. Chem. Phys. **87**, 1355 (1987).
[17] H. Chew, Phys. Rev. A **38**, 3410 (1988).
[18] H. T. Dung, L. Knöll, and D.-G. Welsch, Phys. Rev. A **62**, 053804 (2000).
[19] H. T. Dung, L. Knöll, and D.-G. Welsch, Phys. Rev. A **64**, 013804 (2001).
[20] L. A. Blanco and F. J. García de Abajo, Phys. Rev. B **69**, 205414 (2004).
[21] J. P. Dowling and C. M. Bowden, Phys. Rev. A **46**, 612 (1992).

[22] K. Busch, N. Vats, S. John, and B. C. Sanders, Phys. Rev. E **62**, 4251 (2000).
[23] Y. Yang and S.-Y. Zhu, Phys. Rev. A **62**, 013805 (2000).
[24] D. P. Fussell, R. C. McPhedran, and C. Martijn de Sterke, Phys. Rev. E **72**, 046605 (2005).
[25] D. P. Fussell, R. C. McPhedran, and C. Martijn de Sterke, Phys. Rev. E **70**, 066608 (2004).
[26] A. F. Koenderink, L. Bechger, A. Lagendijk, and W. L. Vos, Phys. Status Solidi A **197**, 648 (2003).
[27] P. Lodahl, A. Floris Van Driel, I. S. Nikolaev, A. Irman, K. Overgaag, D. Vanmaekelbergh, and W. L. Vos, Nature (London) **430**, 654 (2004).
[28] D. L. Andrews and A. A. Demidov (editors), *Resonance Energy Transfer* (Wiley, New York, 1999).
[29] T. Förster, Ann. der Phys. **2**, 55 (1948).
[30] L. Gomberoff and E. A. Power, Proc. Phys. Soc. **88**, 281 (1966).
[31] M. Cho and R. L. Silbey, Chem. Phys. Lett. **242**, 291 (1995).
[32] M. J. A. de Dood, J. Knoester, A. Tip, and A. Polman, Phys. Rev. B **71**, 115102 (2005).
[33] G. S. Agarwal and S. Dutta Gupta, Phys. Rev. A **57**, 667 (1998).
[34] P. Andrew and W. L. Barnes, Science **290**, 785 (2000).
[35] T. Kobayashi, Phys. Lett. A **199**, 21 (1995).
[36] T. Kobayashi, Q. Zheng, and T. Sekiguchi, Phys. Rev. A **52**, 2835 (1995).
[37] D. M. Basko, F. Bassani, G. C. La Rocca, and V. M. Agranovich, Phys. Rev. B **62**, 015962 (2000).
[38] D. M. Basko, G. C. La Rocca, F. Bassani, and V. M. Agranovich, Phys. Status Solidi A **190**, 379 (2002).
[39] V. V. Klimov and V. S. Letokhov, Phys. Rev. A **58**, 3235 (1998).
[40] H. Fujiwara, K. Sasaki, and H. Masuhara, ChemPhysChem **6**, 2410 (2005).
[41] S. D. Druger, S. Arnold, and L. M. Folan, J. Chem. Phys. **87**, 2649 (1987).
[42] F. Le Kien, S. Dutta Gupta, K. P. Nayak, and K. Hakuta, Phys. Rev. A **72**, 063815 (2005).
[43] C. A. Marocico and J. Knoester, Phys. Rev. A **79**, 053816 (2009).
[44] G. S. Agarwal, Phys. Rev. A **11**, 230 (1975); **11**, 243 (1975); **11**, 253 (1975); **12**, 1475 (1975); **12**, 1974 (1975); **12**, 1987 (1975).
[45] H. T. Dung, S. Y. Buhmann, L. Knöll, D.-G. Welsch, S. Scheel, and J. Kästel, Phys. Rev. A **68**, 043816 (2003).
[46] H. T. Dung, L. Knöll, and D.-G. Welsch, Phys. Rev. A **65**, 043813 (2002).
[47] W. C. Chew, *Waves and Fields in Inhomogeneous Media* (IEEE Press, New York, 1994).
[48] S. Barnett, B. Huttner, R. Loudon, and R. Matloob, J. Phys. B **29**, 3763 (1996).
[49] C. T. Tai, *Dyadic Green Functions in Electromagnetic Theory* (IEEE Press, New York, 1994).
[50] B. Gough, *GNU Scientific Library Reference Manual*, 3rd ed. (Network Theory, Bristol, UK, 2009).
[51] A. K. Abdelmageed and A. A. K. Mohsen, Microw. Opt. Tech. Lett. **29**, 130 (2001).
[52] P. B. Johnson and R. W. Christy, Phys. Rev. B **6**, 4370 (1972).
[53] V. M. Agranovich and A. A. Maradudin (editors) *Surface Polaritons: Electromagnetic Waves at Surfaces and Interfaces* (North-Holland, Amsterdam, 1982).
[54] J. A. Dionne, L. A. Sweatlock, H. A. Atwater, and A. Polman, Phys. Rev. B **72**, 075405 (2005).
[55] J. A. Dionne, L. A. Sweatlock, H. A. Atwater, and A. Polman, Phys. Rev. B **73**, 035407 (2006).
[56] G. Ford and W. Weber, Phys. Rep. **113**, 195 (1984).
[57] R. Ortuño, C. García-Meca, F. J. Rodríguez-Fortuño, J. Martí, and A. Martínez, Phys. Rev. B **79**, 075425 (2009).
[58] E. N. Economou, Phys. Rev. **182**, 539 (1969).